Analyzing power measurements for the $\vec{d}+d\rightarrow d+p+n$ breakup reaction at 12 MeV

P. D. Felsher,* C. R. Howell, W. Tornow, M. L. Roberts,† J. M. Hanly,‡ G. J. Weisel, M. Al Ohali, and R. L. Walter
Duke University and Triangle Universities Nuclear Laboratory, Durham, North Carolina 27708-0308

I. Šlaus
Rudjer Boškovic Institute, Zagreb, Croatia
and Triangle Universities Nuclear Laboratory, Durham, North Carolina 27708-0308

J. M. Lambert and P. A. Treado§
Department of Physics, Georgetown University, Washington, D.C. 20057

G. Mertens
University of Tübingen, Tübingen, Germany

A. C. Fonseca
Centro Fisica Nuclear da Universidade de Lisboa, Avenida Professor Gama Pinto, 2, P-1699 Lisbon, Portugal

A. Soldi and B. Vlahovic
North Carolina Central University, Durham, North Carolina 27707
(Received 11 July 1996; revised manuscript received 1 April 1997)

We report the most extensive set of vector iT_{11} and tensor T_{20} and T_{22} analyzing-power data for the $\vec{d}+d\rightarrow d+p+n$ reaction. Two-particle coincidence data have been measured for six deuteron-proton, three deuteron-neutron and three proton-neutron angle pairs at an incident deuteron energy of 12.0 MeV. These data are compared to impulse-approximation calculations that treat the underlying nucleon-deuteron system exactly and include contributions from both target and projectile breakup processes. This model gives a good description of the analyzing-power and relative cross-section data. We show that the inclusion of nucleon-nucleon P interactions considerably improves the agreement with the spin observables. The disagreement between the data and theoretical predictions show the limitations in our model and the importance of the rescattering processes. We suggest that the $d+d$ three-body breakup process will provide useful information on the nucleon-nucleon force when exact calculations become available. [S0556-2813(97)02907-5]

PACS number(s): 24.70.+s, 25.45.−z, 21.45.+v, 25.10.+s

I. INTRODUCTION

The four-body problem can be treated exactly in terms of two-body interactions using Yakubovsky equations [1] for the wave function components or the Alt, Grassberger, and Sandhas equations [2] for the t matrices. Significant progress has been made in recent years by Fonseca [3], Mdlalose *et al.* [4], and Glöckle and co-workers [5] in developing mathematically rigorous $4N$ calculations. In addition, models based on resonating group theory [6], R-matrix analysis [7], the Green function Monte Carlo method [8], and the correlated hyperspherical harmonic expansion method [9] have been developed and are being used to study $4N$ reaction dynamics. Just as is the situation with the three-nucleon ($3N$) system, with improved calculations, the $4N$ system could be used to probe many-nucleon forces and parts of the two-nucleon force to which there is little or no sensitivity in $2N$ systems, e.g., details of the on-shell P interactions at low energies and off-shell force components [10].

Though the rate of progress is encouraging, calculations of scattering observables in the $4N$ system are still quite rudimentary relative to those in the $3N$ system [5,9,11,12]. Specifically, there are no calculations which solve the $4N$ problem exactly at energies above the deuteron breakup threshold. Until now, impulse-approximation (IA) calculations have been used to study the $d+d\rightarrow d+p+n$ breakup reaction [13–16]. Extensive IA analyses of cross-section data [13–23] over a period of three decades have revealed some interesting features of this reaction in the kinematic region of deuteron-nucleon (dN) quasifree scattering (QFS). One important feature that simplifies modeling of the reaction is that the normally dominant $^1S_0$ neutron-proton final-state interaction (FSI) is suppressed in the three-body $d+d$ breakup reaction by isospin conservation. Also, contrary to intuition, at low energies where rescattering is expected to be important because the de Broglie wavelength of the incident deuteron is larger than the size of the target deuteron, IA calculations give a good description of the shape of differential cross-section data for dN QFS. A conclusion drawn from

*Present address: EG&G Rocky Flats, Golden, CO 80402-0464.
†Present address: Lawrence Livermore National Laboratory, Livermore, CA 94550.
‡Present address: Booz, Allen and Hamilton, Huntsville, Alabama 35806.
§Deceased.

 © 1997 The American Physical Society

these results was that the rescattering terms, which must be important at low energies, can be compensated for in IA calculations in one of two ways: either by scaling the deuteron wave function with an energy-dependent normalization factor smaller than 1, or by applying a cutoff of the deuteron wave function at short distances. Both solutions provide intuitive insight about the reaction. The first suggests that the rescattering processes interfere destructively with the leading term of the scattering series. The second emphasizes the peripheral nature of the collisions between the two deuterons at low energy by nullifying the inner part of the deuteron wave function. The reduced importance of the interior of the deuteron wave function can be interpreted as a result of the rescattering processes.

Experimental studies show that in the energy range from 5 to 50 MeV, the dominant processes in the three-body $d+d$ breakup reaction are four QFS poles: the spectator particle is either a neutron or proton in either the target or projectile [13–24]. Measurements using a multidetector system and covering a solid angle of almost 4π showed that a very large fraction of the total cross section is associated with these four poles [13]. However, in all cases, an empirically determined normalization factor of magnitude about 0.1 was needed to bring the predictions of IA calculations into agreement with measured two-particle cross sections. The normalization factor was found to be slightly angle dependent and had to be adjusted for each particle angle pair at each incident deuteron energy [15]. The agreement between IA calcluations and three-body $d+d$ breakup data for QFS kinematics has been improved by including a term to account for the $^3S_1$ neutron-proton (np) FSI, by using a radial cutoff parameter in the deuteron wave function to emphasize the peripheral nature of the QFS process, and by allowing for interference between the poles [15].

As suspected, the need for an overall normalization factor (or a radial cutoff parameter) to bring the IA calculations into agreement with data suggests that rescattering effects are important in the $d+d$ breakup reaction at low energies. However, studying the role of rescattering processes with only cross sections is of limited value and can be misleading as was found in the case of NN QFS in the nd breakup reaction [25]. Prior to the present work at TUNL, a large number of cross-section studies for the $d+d$ breakup reaction had been reported, but only one study of the vector analyzing power [26] has been performed. Additional studies that combine the analysis of cross sections and spin observables are needed to gain insight into the reaction mechanisms for $d+d$ breakup. In this paper, we report an extensive set of measurements of vector and tensor analyzing powers and relative cross sections for the $\vec{d}+d\rightarrow d+p+n$ reaction at an incident deuteron energy of 12.0 MeV. The earlier paper of Howell *et al.* [27] reported a subset of the data to be presented here. The data are compared to our newly developed model which is built in the spirit of the IA. In the sections to follow, we describe the experimental setup and techniques used to acquire the data, the formulation of our IA model, and the results of the comparisons of the IA calculations to our data.

II. EXPERIMENTAL DETAILS

The experimental setup and techniques used in the present work are the same as those reported in Refs. [27,28]. The

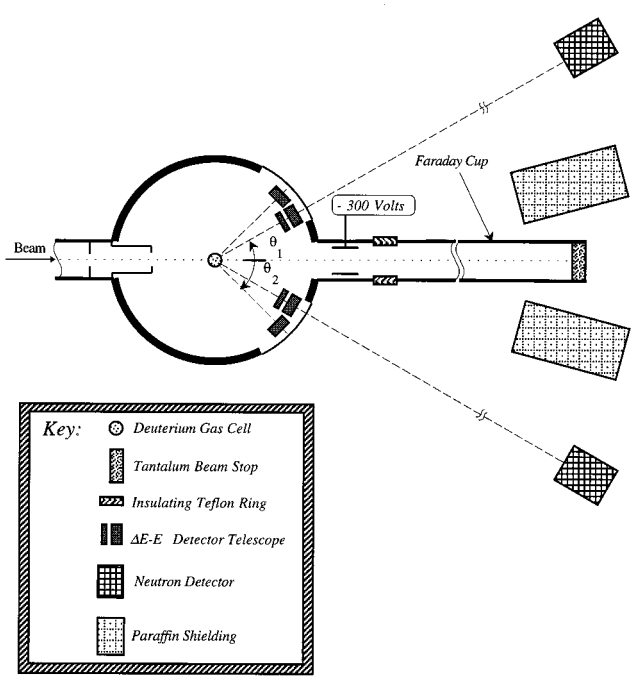

FIG. 1. Schematic top view of the experimental setup for the $\vec{d}+d\rightarrow d+p+n$ breakup measurements. This drawing is not to scale. Detector dimensions and distances are given in the text.

experimental setup is shown in Fig. 1. The experiment was designed to simultaneously measure analyzing-power data for deuteron-proton (dp), deuteron-neutron (dn), and proton-neutron (pn) coincidences. All measurements were made using a gas target. The target cell was a right cylinder with a diameter of 2.5 cm. The cell was oriented vertically, such that its axis was perpendicular to the beam axis. The gas was contained by an 8-μm-thick uncoated Kapton foil, and the cell was pressurized to 1.0 atm. The energy of the incident deuteron beam at the center of the cell was 12.0 MeV. The polarized deuteron beam was produced by the TUNL Lamb-Shift polarized ion source [29]. Two sets of slits upstream of the scattering chamber defined a beam spot on target of about 1 mm^2. The beam was stopped in an electrically isolated tantalum disk, which was connected to a current integrator for measurement of the accumulated charge on target. Silicon surface barrier detectors were used to measure the energy and type of the ejected charged particles, and the neutrons were detected using liquid organic scintillators. The dc polarized beam current on target was kept below about 25 nA as a compromise between coincidence counting rate, signal pileup in the silicon detectors, and heating of the Kapton containment foil.

The liquid organic scintillators were rectangular in shape (7.62-cm wide$\times$15.24-cm high$\times$10.16-cm thick). The center-to-center distance between the deuterium gas target and each neutron detector was 2.65 m. The detectors were shielded from the beam stop on both sides of the beam axis by a 50-cm-thick stack of lithium-loaded paraffin blocks. The scattering chamber had a thin window, 0.64-mm-thick stainless steel, in the forward angular region from 16° to 40° on each side of the incident beam axis to reduce attenuation of the ejected neutrons in the angular range of interest. The rest of the chamber wall was made of 1-cm-thick alu-

TABLE I. Coincidence angle pairs measured and data accumulation time for each pair.

Detected particles	Angles	Time (h) iT_{11} and T_{22}	Time (h) T_{20}
deuteron, proton	$\pm 10.0, \mp 10.0$	105	45
deuteron, proton	$\pm 10.0, \mp 41.2$	105	45
deuteron, proton	$\pm 17.0, \mp 17.0$	270	235
deuteron, proton	$\pm 17.0, \mp 34.5$	110	60
deuteron, proton	$\pm 19.4, \mp 19.4$	85	95
deuteron, proton	$\pm 34.5, \mp 17.0$	110	60
deuteron, neutron	$\pm 17.0, \mp 17.0$	70	105
deuteron, neutron	$\pm 17.0, \mp 34.5$	90	75
deuteron, neutron	$\pm 19.4, \mp 28.9$	85	95
proton, neutron	$\pm 17.0, \mp 17.0$	70	105
proton, neutron	$\pm 17.0, \mp 34.5$	90	75
proton, neutron	$\pm 19.4, \mp 28.9$	85	95

mium. Liquid scintillators were preferred over plastics because of their γ-ray suppression capability using pulse-shape techniques. The γ-ray rejection in our measurements was about 20:1, i.e., about 95% of the γ-ray interactions in the liquid scintillators were rejected.

The detectors were positioned to measure the momentum of two of the emitted particles. A standard right-handed coordinate system was used, and the polar and azimuthal scattering angles θ and ϕ were defined in the usual way (θ is measured from the $+z$ axis to the particle momentum vector and ϕ is measured up from the $+x$ axis to the plane containing the particle momentum vector and the $+z$ axis). The $+z$ axis was along the incident beam and the $+y$ axis pointed up from the horizontal scattering plane. Since, the center of each detector was located in the horizontal scattering plane, the azimuthal scattering angle was either $\phi = 0°$ or $\phi = 180°$. For compactness of notation, we shall refer to the scattering angles (θ,0°) and (θ,180°) as $+\theta$ and $-\theta$, respectively. To reduce instrumental errors in the asymmetry measurements, the detector pairs were symmetrically placed about the beam axis, and the coincidence yields from the symmetric pairs were averaged geometrically [30]. For instance, the analyzing powers for the dp coincidence measurements were obtained from the averaged yields of the ($\theta_d = +17°$, $\theta_p = -17°$) and ($\theta_d = -17°$, $\theta_p = +17°$) detector-angle pairs. The angle pairs measured and the data acquisition times for each pair are listed in Table I. The charged-particle detectors positioned at 10.0°, 17.0°, and 19.4° were ΔE-E telescopes and were used to determine the momentum and type of each detected particle. The angular acceptance of each silicon detector was defined by a set of double rectangular collimators. The polar and azimuthal angular acceptances of the charged-particle detectors were $\pm 1.0°$ and $\pm 4.1°$, respectively. The acceptances of the neutron detectors were $\Delta\theta = \pm 0.9°$ and $\Delta\phi = \pm 5.7°$.

For each detector, two independent two-particle coincidence circuits were used to generate the event triggers: one for measuring the foreground (true and accidental events) and the other for measuring the background due to *accidental* coincidences. Since a foreground trigger can be caused by either a true or false two-particle coincidence, we shall refer to the events associated with foreground trigger signals as *true+accidental* events. The trigger signals for purely *accidental* events were generated by delaying the signals from one detector by an additional 300 ns beyond the time offset needed for coincidence timing.

TABLE II. Beam conditions for the T_{20} measurements. The angles β and γ are defined in text.

Data step	β(deg.)	γ(deg.)	Spherical $(\tau_{10})_{max}$	Spherical $(\tau_{20})_{max}$
1	0	undefined	$\sqrt{\frac{3}{2}}$	$\frac{1}{\sqrt{2}}$
2	180	undefined	$\sqrt{\frac{3}{2}}$	$\frac{1}{\sqrt{2}}$
3	180	undefined	0	$-\sqrt{2}$
4	0	undefined	0	$-\sqrt{2}$

All measurements were made using a four-step sequence consisting of two values of the beam polarization moments with a reversal of the direction of the spin quantization axis $\hat{\mathbf{s}}$ for each moment setting. The T_{20} measurements were made independent of those for iT_{11} and T_{22}. The beam moments and the $\hat{\mathbf{s}}$ direction for the T_{20} measurements are given in Table II, and the beam conditions used in the iT_{11} and T_{22} measurements are shown in Table III. The τ_{10} and τ_{20} are the vector and tensor beam moments [31]. The actual beam polarization was about 70% of the maximum values listed in Tables II and III and was determined using the quench-ratio method [32]. The angle β is between the $\mathbf{k}_{in}$ and $\hat{\mathbf{s}}$ vectors, and γ is the angle between the unit normal vector $[(\mathbf{k}_{in} \times \mathbf{k}_{out}) / |\mathbf{k}_{in} \times \mathbf{k}_{out}|]$ and the plane containing $\mathbf{k}_{in}$ and $\hat{\mathbf{s}}$. The vector $\mathbf{k}_{in}$ is the momentum vector of the incident deuteron, in the $+z$ direction by convention of our coordinate system and $\mathbf{k}_{out}$ is the momentum vector of the outgoing deuteron in the d-N coincidences and of the emitted proton in the case of p-n coincidences.

For each step, the events from each two-particle coincidence were sorted into two-dimensional histograms of E_1 (the energy of the particle emitted at angle θ_1) versus E_2 (the

TABLE III. Beam conditions for the iT_{11} and T_{22} measurements. The angles β and γ are as defined in text.

Data step	β(deg.)	γ(deg.)	Spherical $(\tau_{10})_{max}$	Spherical $(\tau_{20})_{max}$
1	90	0	$\sqrt{\frac{3}{2}}$	$\frac{1}{\sqrt{2}}$
2	90	180	$\sqrt{\frac{3}{2}}$	$\frac{1}{\sqrt{2}}$
3	90	180	0	$-\sqrt{2}$
4	90	0	0	$-\sqrt{2}$

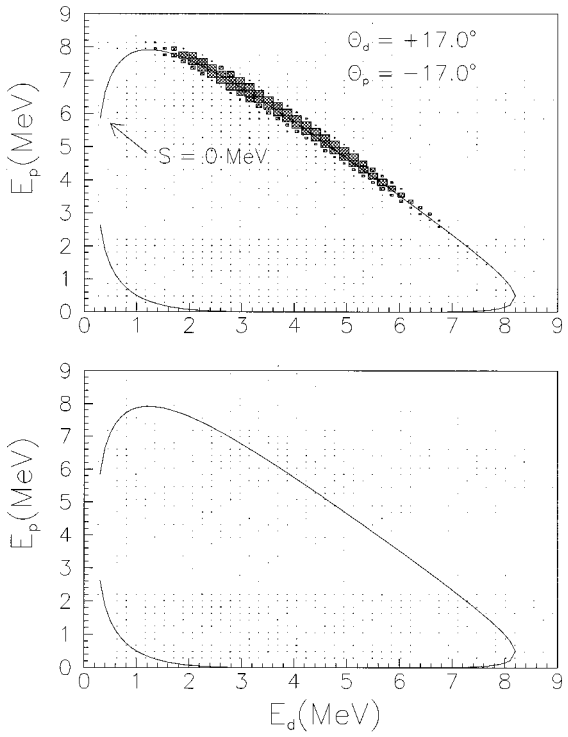

FIG. 2. Two-dimensional histogram of the detected deuteron energy E_d at $\theta_d = +17°$ vs the energy of the detected proton E_p at $\theta_p = -17°$. The top histogram was accumulated using the *true +accidental* triggers, and the counts in the bottom histogram are due solely to *accidental* coincidences. The curve is the point-geometry kinematic locus for the breakup reaction.

energy of the particle emitted at angle θ_2). Separate histograms were accumulated for events from foreground and background triggers. The gain of each silicon detector and the beam polarization were monitored using single-detector event data. The ΔE-E telescopes were used for charged-particle identification at 10.0°, 17.0°, and 19.4°. A histogram of deuteron energy (E_d) versus proton energy (E_p) for d-p coincidence events for the angle pair at $(\theta_d, \theta_p) = (+17.0°, -17.0°)$ is shown in Fig. 2. The counts in the top histogram are due to *true+accidental* coincidences, and the bottom histogram contains only counts due to *accidental* coincidences. The intensity scale is the same for both histograms. The curve is the point-geometry kinematic locus for the breakup reaction and is generally referred to as the S curve. As shown in Fig. 2, the S value is defined to be zero at the minimum energy of particle one, and the value of S increases as one moves clockwise along the kinematic locus. The data are smeared about the S curve due the energy and angular spread in our experimental setup. The angular acceptances were discussed above, and the energy spreads have been reported in detail by Howell *et al.* [27]. The experimental energy spread was dependent on the energy and type of the detected particle. The energy of the detected deuterons ranged from 8 MeV down to the threshold of our detectors, about 2 MeV; the respective mean energy spreads ranged from 45 to 85 keV. The mean energy spread in the detected protons in the same energy range was slightly less, 30 to 50 keV. These energy spreads include the 20 keV intrinsic energy resolution of the silicon detectors. The energy of each detected neutron was determined from the the neutron time-of-flight (TOF). The neutron TOF was derived from three measured quantities: the time difference between the detection of the neutron and the associated charged particle, the energy and type of the charged particle (measured using the ΔE-E telescope), and the flight-path lengths of the charged particle and the neutron. The spread in the measured neutron energy was mainly due to the intrinsic time resolution ($\Delta t = 1.5$ ns) of the neutron detector and the flight path dispersion caused by the finite extent of the gas target and the thickness of the neutron detector. The spread in the detected neutron energy ranged from 200 to 730 keV for neutron energies between 2 and 8 MeV, respectively.

The counts in the E_1 vs E_2 histograms were projected onto the S curve using the minimum distance technique [27]. Data were acquired for 15 min in each step and the four-step sequence was repeated until the desired statistical accuracy was achieved. The data were summed into 750-keV bins along the S curve. After subtraction of the accidental background, as described by Howell *et al.* [27], the analyzing powers were computed from the *true-coincidence* counts in each bin of the four S curve distributions resulting from the four-step measurement sequence. The yields for a particular (θ_1, θ_2, S) value for the $\vec{d}+d \rightarrow d+p+n$ breakup reaction using a polarized beam can be written for a coplanar geometry as [33]

$$N(\theta_1,\theta_2,S) = N_o(\theta_1,\theta_2,S)\left\{1+\sqrt{2}\,\tau_{10} iT_{11}\sin\beta\,\cos\gamma + \frac{1}{2}\,\tau_{20}\,T_{20}(3\cos^2\beta-1) + \sqrt{6}\,\tau_{20}T_{21}\sin\beta\,\cos\beta\,\sin\gamma - \sqrt{\frac{3}{2}}\,\tau_{20}T_{22}\sin^2\beta\,\cos 2\gamma\right\}. \quad (1)$$

The $N_o(\theta_1, \theta_2, S)$ in the above equation is the yield obtained with an unpolarized beam. The iT_{11}, T_{20}, and T_{22} are the vector and tensor analyzing powers for the kinematic point defined by θ_1, θ_2, and S. The four-step sequences given in Tables II and III result in four equations which were used to solve for the analyzing powers iT_{11}, T_{20}, and T_{22} in Eq. (1). The tensor analyzing power T_{21} was not measured because of our choices of β and γ.

III. THEORY

Before realistic $3N$ calculations were available, nucleon-deuteron (Nd) vertices in impulse-approximation (IA) calculations were evaluated using elastic scattering Nd cross-section data. That approach had two shortcomings. First, it ignored the off-shell contributions to the QFS amplitudes. This neglect has been shown to have important consequences on the calculated cross section [34]. Second, and more importantly, using Nd data inherently does not include the interference between poles. In our calculations, reliable representations of the $3N$ subsystems are achieved by using separable NN interactions to exactly compute the Nd vertices. Only neutron-deuteron (nd) amplitudes are used, and no attempt is made to include the Coulomb-force effects.

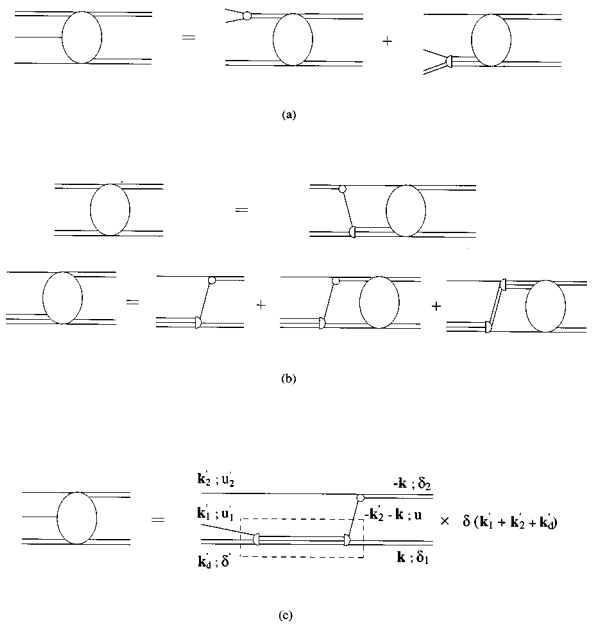

FIG. 3. Graphical representations of the effective two-body equations for: (a) the full $d+d\to d+p+n$ three-body breakup amplitude; (b) the $2+2\to 2+2$ and $2+2\to 1+3$ amplitudes; and (c) the lowest order diagram in the Born series expansion of the breakup amplitude and kinematic parameters used to describe the system.

Charge independence is imposed in all states of the NN forces.

Since $d+d\to d+p+n$ cross-section data suggest that dN QFS is the dominant feature of the reaction, we develop, in the spirit of the impulse approximation, a model which is the coherent sum of four terms: dn and dp QFS scattering with one nucleon in either the target or the projectile behaving as a spectator. In effect, it may be easily shown that these four terms correspond to the lowest order diagrams in the Born series expansion of the t matrix for the $d+d\to n+p+d$ reaction. In the framework of the AGS equations [2], the breakup amplitude shown in Fig. 3(a) may be written as the sum of two terms involving both the $2+2\to 2+2$ and $2+2\to 1+3$ half-shell amplitudes, which may be obtained from the solution of the set of coupled integral equations shown diagramatically in Fig. 3(b). Although these diagrams result from the quasiparticle representation of all subsystem amplitudes in the original AGS equation, they remain general enough to provide physical insight into four-particle dynamics. If one takes the lowest order diagram in the Born series expansion of the integral equation shown diagramatically in Fig. 3(b), the $2+2\to 2+2$ amplitudes become zero and the $2+2\to 1+3$ amplitudes consist solely of the one-nucleon exchange term. Once this approximation is carried out in the equation for the breakup amplitude, shown in Fig. 3(a), one gets the lowest order diagram for the breakup amplitude shown in Fig. 3(c). Inside the dashed rectangle in Fig. 3(c) one may identify the $3N$ scattering amplitude for $1+2\to 1+2$ embedded in four-particle space through an energy shift that equals the kinetic energy of the spectator nucleon relative to the center of mass of the underlying $3N$ subsystem. The symmetrization of the diagram in Fig. 3(c) results in four terms due to the interchange of the two deuterons in the initial state and the two nucleons in the final state. Denoting the $3N$ t matrix as Z, one may write the breakup amplitude T using the kinematics notation of Fig. 3(c) together with the appropriate magnetic quantum numbers for all the particles involved:

$$\begin{aligned} T&=\langle 1\,\delta'\mathbf{k}'_d;\tfrac{1}{2}\,u'_1\mathbf{k}'_1;\tfrac{1}{2}\,u'_2\mathbf{k}'_2|T(E)|1\,\delta_1\mathbf{k};1\,\delta_2-\mathbf{k}\rangle \\ &\quad\times\delta(\mathbf{k}'_1+\mathbf{k}'_2+\mathbf{k}'_d) \\ &=T_1+T_2, \end{aligned} \tag{2}$$

$$\begin{aligned} T_1=\frac{1}{\sqrt{2}}\Big\{&\langle 1\,\delta'\,\tfrac{1}{2}\,u'_2;\mathbf{Q}'_1|Z(\varepsilon_1)|\mathbf{Q}_1^+;1\,\delta_2\,\tfrac{1}{2}\,u\rangle \\ &\times\chi_d\left[\mathbf{q}_1^+;\begin{pmatrix}\frac{1}{2}&\frac{1}{2}\\ u&u'_1\end{pmatrix}\begin{pmatrix}s&l\\ s_z&m\end{pmatrix}\begin{matrix}1\\ \delta_1\end{matrix}\right] \\ &+\langle 1\,\delta'\,\tfrac{1}{2}\,u'_2;\mathbf{Q}'_1|Z(\varepsilon_1)|\mathbf{Q}_1^-;1\,\delta_2\,\tfrac{1}{2}\,u\rangle \\ &\times\chi_d\left[\mathbf{q}_1^-;\begin{pmatrix}\frac{1}{2}&\frac{1}{2}\\ u&u'_1\end{pmatrix}\begin{pmatrix}s&l\\ s_z&m\end{pmatrix}\begin{matrix}1\\ \delta_1\end{matrix}\right], \end{aligned} \tag{3}$$

$$\begin{aligned} T_2=\frac{1}{\sqrt{2}}\Big\{&\langle 1\,\delta'\,\tfrac{1}{2}\,u'_1;\mathbf{Q}'_2|Z(\varepsilon_2)|\mathbf{Q}_2^+;1\,\delta_1\,\tfrac{1}{2}\,u\rangle \\ &\times\chi_d\left[\mathbf{q}_2^+;\begin{pmatrix}\frac{1}{2}&\frac{1}{2}\\ u&u'_2\end{pmatrix}\begin{pmatrix}s&l\\ s_z&m\end{pmatrix}\begin{matrix}1\\ \delta_2\end{matrix}\right] \\ &+\langle 1\,\delta'\,\tfrac{1}{2}\,u'_1;\mathbf{Q}'_2|Z(\varepsilon_2)|\mathbf{Q}_2^-;1\,\delta_1\,\tfrac{1}{2}\,u\rangle \\ &\times\chi_d\left[\mathbf{q}_2^-;\begin{pmatrix}\frac{1}{2}&\frac{1}{2}\\ u&u'_2\end{pmatrix}\begin{pmatrix}s&l\\ s_z&m\end{pmatrix}\begin{matrix}1\\ \delta_2\end{matrix}\right]\Big\}, \end{aligned} \tag{4}$$

where χ_d is the deuteron wave function and

$$\mathbf{Q}'_i=-\tfrac{2}{3}\,\mathbf{k}'_i-\mathbf{k}'_d, \tag{5}$$

$$\mathbf{Q}_i^{\pm}=-\tfrac{2}{3}\,\mathbf{k}'_i\mp\mathbf{k}, \tag{6}$$

$$\mathbf{q}_i^{\pm}=\mathbf{k}'_i\pm\tfrac{1}{2}\,\mathbf{k}, \tag{7}$$

$$\varepsilon_i=E-\tfrac{4}{3}\,k_i'^2, \tag{8}$$

$$E+2\epsilon_d-k^2=0, \tag{9}$$

$$E+\epsilon_d-k_1'^2-k_2'^2-\frac{k_d'^2}{2}=0, \tag{10}$$

in units of $\hbar=m_Nc^2=1$, where m_N is the mass of the nucleon. In the above equations and in Fig. 3, the δ_1 and δ_2 represent the magnetic spin projections of the two deuterons in the incident channel and the δ' is the magnetic spin projection of the exit-channel deuteron. The magnetic spin projections of the transfered nucleon and the ejected nucleons are u, u'_1, and u'_2, respectively. All momenta are computed in the $d+d$ c.m. reference frame. The momenta of the incident and ejected deuterons are represented by $\mathbf{k}$ and $\mathbf{k}'_d$,

and the momenta of the emitted nucleons are denoted by $\mathbf{k}_1'$ and $\mathbf{k}_2'$. In all calculations, we use a momentum-space Hulthen deuteron wave function with a smooth radial cutoff [15]. The parameters of the wave function were $\alpha=45$ MeV/c, $\beta=237.18$ MeV/c, and the radial cutoff parameter $\beta'=84.69$ MeV/c. Since the D-state component of the deuteron wave function is small, less than 7% probability, only the S state was considered to simplify the angular momentum couplings.

Assuming that deuteron ''one'' is the projectile, then T_1 and T_2 in Eq. (2) correspond to projectile and target breakup, respectively. Given the on-shell relation, the $3N$ t matrix $Z(\epsilon_i)$ $(i=1,2)$ is on-shell on the left side and off-shell on the right side in Eqs. (3) and (4). Using Eqs. (5)–(9) one gets

$$\varepsilon_i=E-\tfrac{4}{3}k_i'^2=-\epsilon_d+\tfrac{3}{2}Q_i'^2, \tag{11}$$

while

$$\varepsilon_i\neq-\epsilon_d+\tfrac{3}{2}(\mathbf{Q}_i^{\pm})^2. \tag{12}$$

The tensor observables T_{kq} are computed using the $4N$ amplitudes in Eq. (2):

$$T_{kq}\mathrm{Tr}\{T^\dagger T\}=\mathrm{Tr}\{T^\dagger T\tau_{kq}\} \tag{13}$$

$$=\sum_{\substack{\delta_1\delta_2\\ \delta_1'\delta_2'}}\langle 1\,\delta_1 1\,\delta_2|T^\dagger T|1\,\delta_1' 1\,\delta_2'\rangle \times\langle 1\,\delta_1' 1\,\delta_2'|\tau_{kq}|1\,\delta_1 1\,\delta_2\rangle \tag{14}$$

$$=\sum_{\delta_1\delta_2\delta_1'}\sum_{u_1'u_2'\delta'}\langle 1\,\delta_1 1\,\delta_2|T^\dagger|\tfrac{1}{2}\,u_1'\,\tfrac{1}{2}\,u_2' 1\,\delta'\rangle \times\langle\tfrac{1}{2}\,u_1'\,\tfrac{1}{2}\,u_2' 1\,\delta'|T|1\,\delta_1' 1\,\delta_2\rangle\hat{k}\;C^{1k1}_{\delta_1 q\delta_1'}, \tag{15}$$

where C is a Clebsch-Gordan Coefficient and $\hat{k}=\sqrt{2k+1}$. Equation (13) is expanded and evaluated in the Appendix.

The kinematic variables were evaluated in even steps along the S curve, and for each value of ε_1 and ε_2, the half-shell t matrices for $n+d\rightarrow n+d$ scattering were rigorously calculated using a rank one Yamaguchi separable NN potential for the channels: $^1S_0$, $^3S_1-{}^3D_1$, $^1P_1$, $^3P_0$, $^3P_1$, and $^3P_2$. In each partial wave, the parameters of the NN potential were fitted to low-energy NN data such as phase shifts, scattering lengths, effective ranges, the deuteron binding energy, and the deuteron quadrupole moment. For $^1S_0$ and $^3S_1-{}^3D_1$ force components, we use the parameters of Phillips [35], which correspond to 5.5% D-state in the deuteron, and for the P forces, we use the parameters of Correl *et al.* [36].

IV. RESULTS AND DISCUSSION

Because our model treats the $3N$ subsystems exactly with well developed NN interactions, comparisons of our model calculations to experimental data give a measure of the contributions from the rescattering terms to the full $4N$ breakup amplitude. The consequences of truncating the full $4N$ amplitudes at the leading term will be explored using our relative cross-section and analyzing-power data, and the influence of each Nd vertex on cross sections and analyzing powers will be investigated. Predictions of our model are shown in Figs. 4 and 5 in comparison to our relative cross-section data. The data and calculations are plotted as a function of S, the distance along the kinematical locus as defined in Fig. 2 and described in the experimental section of this paper. Our dn data at $(\theta_d=+17.0°,\ \theta_n=-17.0°)$ and $(\theta_d=+17.0°,\ \theta_n=-34.5°)$ are not shown, since they are almost identical to the dp coincidence data. At each particle angle pair, the calculated cross section is normalized to fit the peak value of the QFS enhancement. As shown in Eqs. (2)–(4), the $4N$ t matrix is determined from the deuteron wave function and the off-shell nd t matrix. The breakup cross section is computed as the square of the $4N$ breakup amplitudes, Eq. (13), and a phase-space factor. The solid curves shown in Figs. 4 and 5 are IA calculations using the complete expression for the $4N$ t matrix in Eq. (2). The dashed curves were produced by switching off the interference between the two complex amplitudes derived from T_1 and T_2 that make up the $4N$ breakup amplitude. The dotted curves are calculations made with T_1 (projectile breakup t matrix) set to zero. Because our model only includes the leading term of the full $4N$ t matrix, its description of $d+d$ breakup observables is expected to be best in a narrow kinematic region around dN QFS. For this reason, we limit our discussions of the comparisons of data and calculations to the 4-MeV region on the S curve centered at the peak of the QFS enhancement. For the dN coincidences, our model predicts almost equal contributions from the target and projectile breakup terms at $(\theta_d=+10.0°,\theta_p=-10.0°)$, $(\theta_d=+17.0°,\ \theta_p=-17.0°)$, $(\theta_d=+19.4°,\ \theta_p=-19.4°)$, and $(\theta_d=+34.5°,\ \theta_p=-17.0°)$. According to the model predictions, the target breakup process is dominant at $(\theta_d=+10.0°,\ \theta_p=-41.0°)$, $(\theta_d=+17.0°,\ \theta_p=-34.5°)$, and $(\theta_d=+19.4°,\ \theta_p=-28.9°)$. In the case of the pn coincidences, the cross section is dominated by projectile breakup. The model gives the best descriptions of the cross-section data at angles where the contributions from both breakup processes are substantial, affirming the importance of the interference between T_1 and T_2. It is somewhat surprising that in the case of the dN coincidences at angles that were chosen to be dominated by one QFS process, the model describes the cross section rather poorly. This is true in particular for the angle pairs of $(\theta_d=+19.4°,\ \theta_p=-28.9°)$ and $(\theta_d=+17.0°,\ \theta_p=-34.5°)$, where the target breakup process contributes more than 80% to the cross section. The reason for this behavior is unclear.

Our vector iT_{11} and tensor T_{20} and T_{22} analyzing-power data are shown in Figs. 6–15 in comparison to our IA calculations. The solid curves are predictions made with a NN force that includes the $^1S_0$, $^3S_1-{}^3D_1$, $^1P_1$, $^3P_0$, $^3P_1$, and $^3P_2$ partial waves. The dashed curves are predictions made without the $^1P_1$ and ^3P_j NN forces. As expected from low-energy nd scattering [37], the iT_{11} is more sensitive to the NN P interactions than the tensor analyzing powers. At all dN coincidence angles, the addition of NN P forces cause the predicted iT_{11} to change sign from negative to positive. However, there are several angles where T_{20} shows significant sensitivity to the P forces. The inclusion of NN P

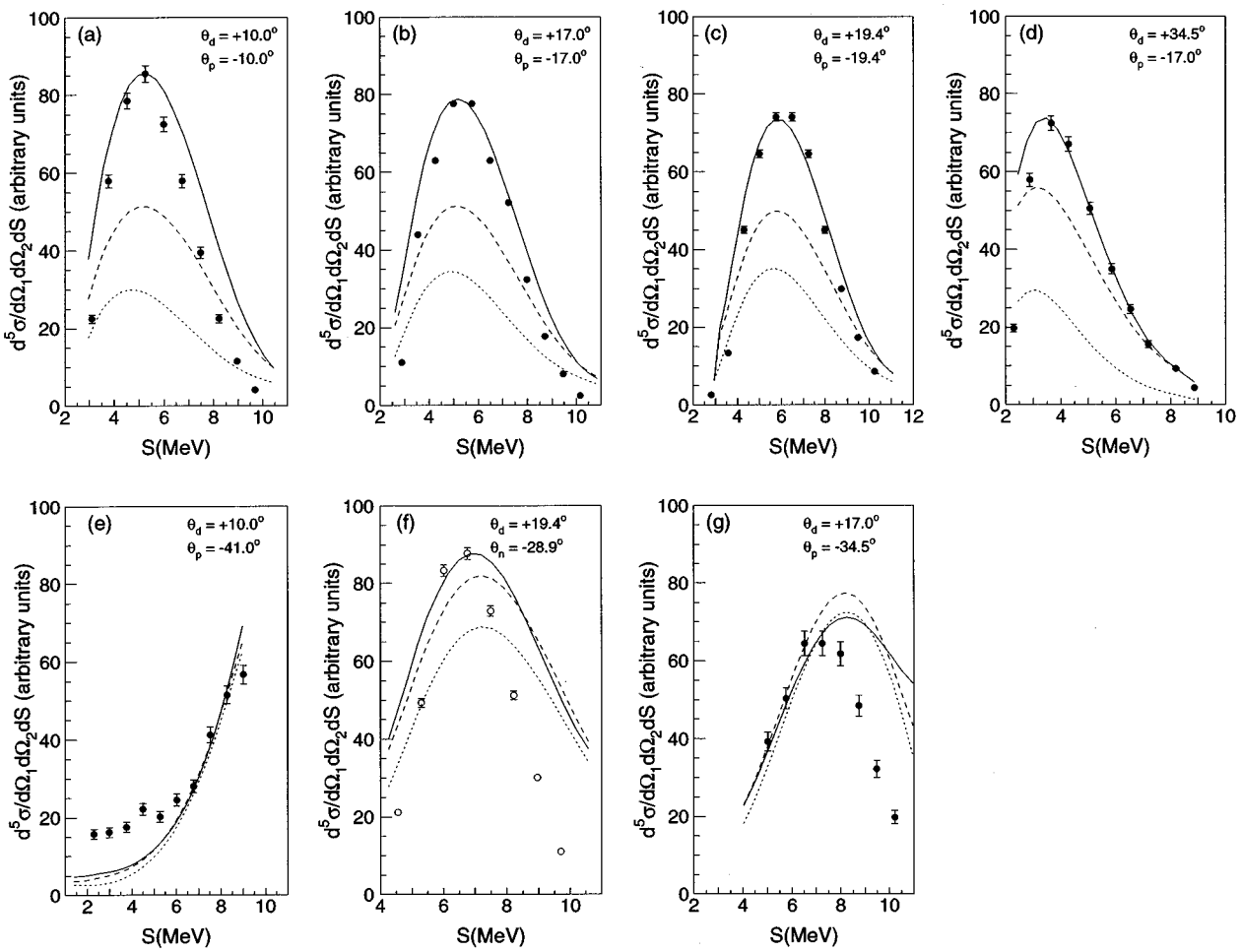

FIG. 4. Relative cross sections for the $d+d\rightarrow d+p+n$ reaction as a function of the arc length S along the E_d vs E_N kinematic locus for an incident deuteron energy of 12.0 MeV. The particle angles are given in the plots. The data are from the present experiment, and the error bars represent only statistical uncertainties. The solid curve is the prediction of our IA model using Eq. (2) for the $4N$ t matrix, the dotted curve is made using only the target breakup term T_2 in Eq. (2), and the dashed curve is a calculation that uses both T_1 and T_2 but does not include interference between the two terms. The full IA calculation was normalized to the maximum in the energy spectrum for each particle angle pair.

forces in our model gives a very good description of the iT_{11} data. The model without NN P forces predicts the wrong sign of iT_{11}. With NN P interactions included, the model gives a better description of the T_{20} data. *The study of vector and tensor analyzing powers is crucial in determining the effects of the inclusion of NN P forces, since the model with and without NN P forces predicts almost identical shapes of the breakup cross sections.* Considering the simplicity of the model, the overall description of the data is impressive.

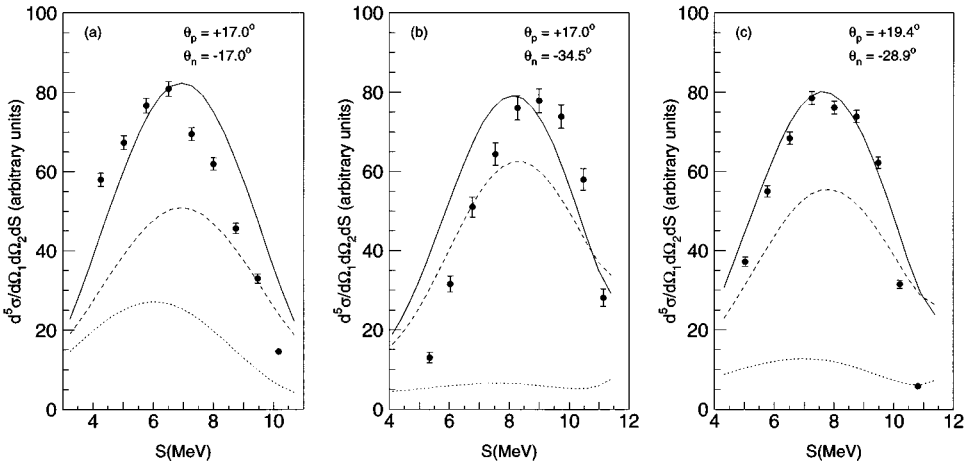

FIG. 5. Same as Fig. 4 except for proton-neutron coincidences. The arc length S is measured along the E_p vs E_n kinematic locus.

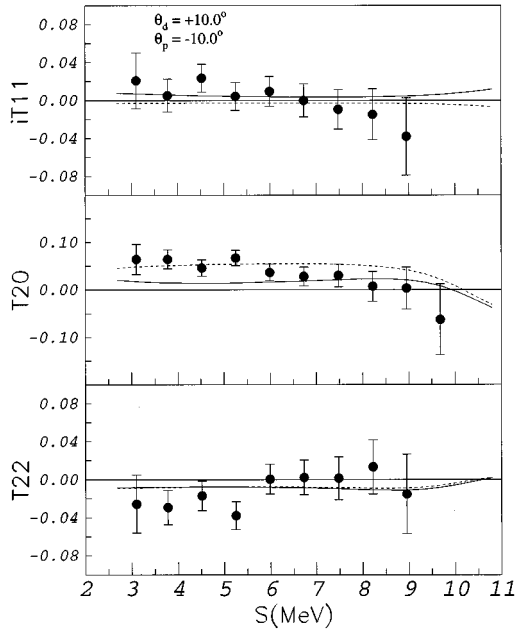

FIG. 6. Analyzing powers for the $\vec{d}+d\rightarrow d+p+n$ reaction at an incident deuteron energy of 12.0 MeV. The arc length S is measured along the E_d vs E_p kinematic locus. The ejectile angles are $\theta_d=+10.0°$ and $\theta_p=-10.0°$. The data are from the present experiment, and the error bars represent only statistical uncertainties. The solid curves are our IA calculations made with the following NN force components: $^1S_0$, $^3S_1-^3D_1$, $^1P_1$, $^3P_0$, $^3P_1$, and $^3P_2$. The dashed curves are the predictions without the $^1P_1$ and ^3P_j NN forces.

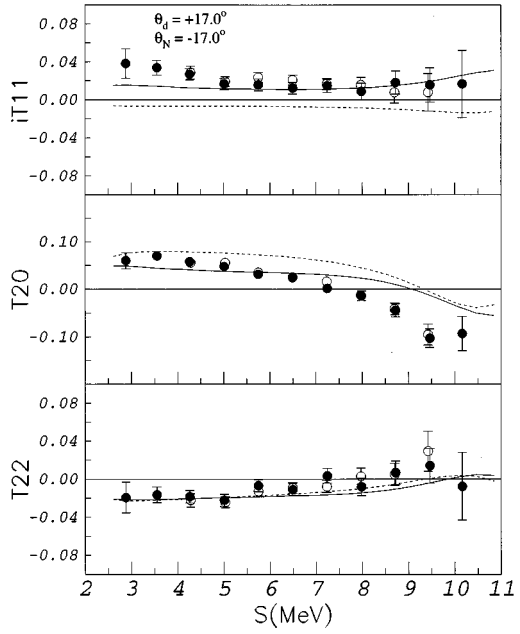

FIG. 7. Analyzing powers for dN coincidences for the $\vec{d}+d\rightarrow d+p+n$ reaction at an incident energy of 12.0 MeV. The particle angles are $\theta_d=+17.0°$ and $\theta_N=-17.0°$. The data are from the present measurements and the solid and open data points are for dp and dn coincidences, respectively. The calculations are the same as in Fig. 6

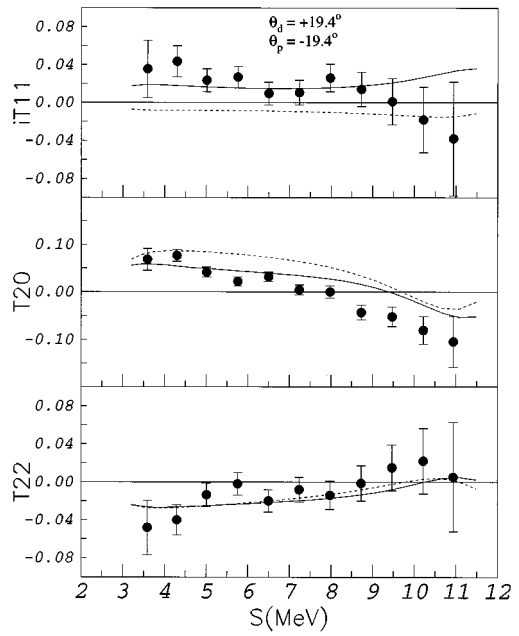

FIG. 8. The same as Fig. 6, except for particle angles $\theta_d=+19.4°$ and $\theta_p=-19.4°$.

After making a global survey, detailed comparisons between data and theory are made for each type of observable. The iT_{11} data are well described except at three angles: $(\theta_d=+34.5°,\theta_p=-17.0°)$, $(\theta_d=+10.0°,\theta_p=-41.2°)$, and $(\theta_p=+17.0°,\theta_n=-17.0°)$. The iT_{11} predictions for $(\theta_d=+34.5°,\theta_p=-17.0°)$ are systematically more positive than the data (see Fig. 9). As shown in Fig. 10, the data for S less than 7 MeV at the angle pair $(\theta_d=+10.0°,\theta_p=-41.2°)$ have an average value of -0.062 ± 0.013 and differ by five standard deviations from the calculations, which are essentially zero. The discrepancy at $(\theta_d=+34.5°,\theta_p=-17.0°)$ may indicate deficiencies in

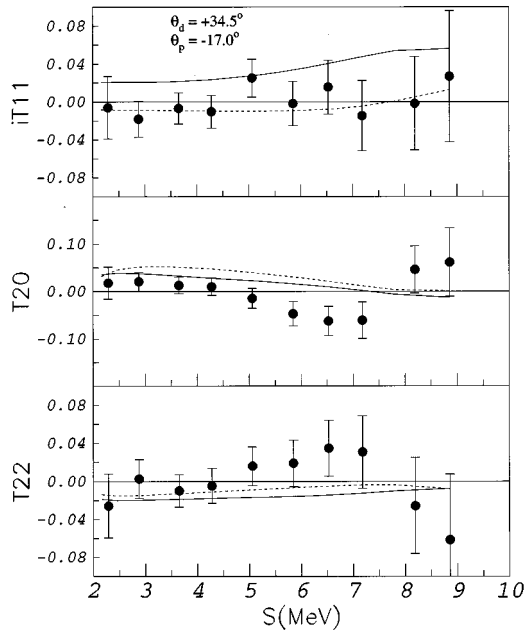

FIG. 9. The same as Fig. 6, except for particle angles $\theta_d=+34.5°$ and $\theta_p=-17.0°$.

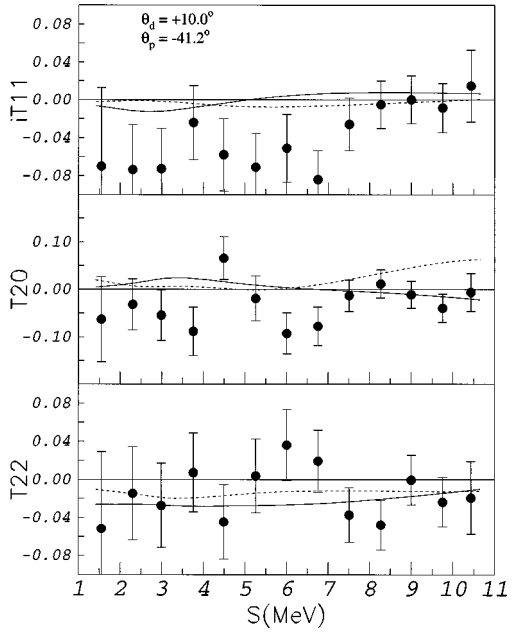

FIG. 10. The same as Fig. 6, except for particle angles $\theta_d = +10.0°$ and $\theta_p = -41.2°$.

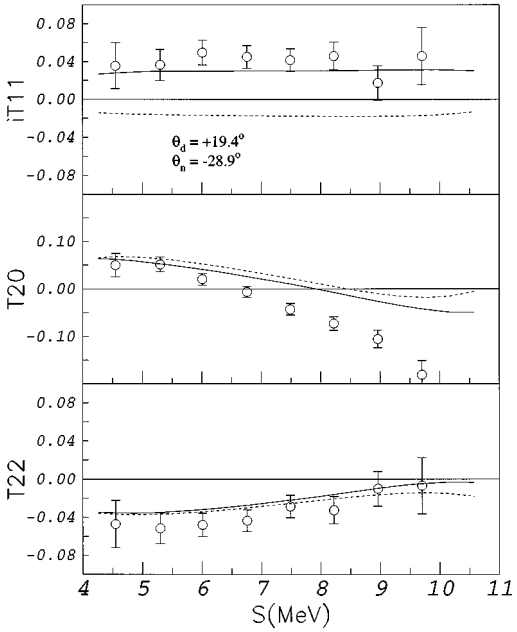

FIG. 12. The same as Fig. 6, except for particle angles $\theta_d = +19.4°$ and $\theta_n = -28.9°$.

the treatment of the P interactions in the model. In contrast, the disagreement between the calculations and data at $(\theta_d = +10.0°, \theta_p = -41.2°)$ for $S < 7$ MeV is most likely caused by the truncation of the scattering series, since iT_{11} shows little sensitivity to NN P interactions at this angle (see Fig. 10) and because the model fails to predict the shape of the cross-section data for S less than 7 MeV, see Fig. 4(e). Shown in Fig. 13, the two failures of the predictions at $(\theta_p = +17.0°, \ \theta_n = -17.0°)$ are that the calculated energy dependence of iT_{11} along S does not match that of the data and the predicted value of iT_{11} at $S = 7$ MeV is zero and about 2.5 standard deviations lower than the data. The

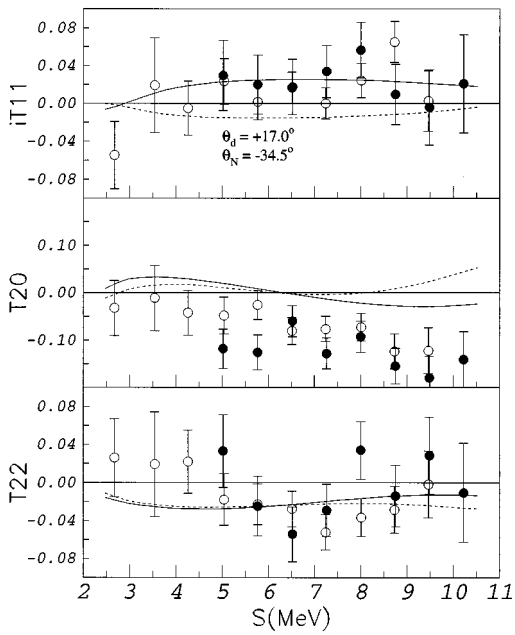

FIG. 11. The same as Fig. 7, except for particle angles $\theta_d = +17.0°$ and $\theta_N = -34.5°$.

disprecancy at $S = 7$ MeV is important because charge symmetry requires iT_{11} to be equal to zero at this point [27].

The model gives a reasonably good description of our tensor analyzing-power data for the dN coincidences. The importance of the NN tensor force in the tensor analyzing powers for the dN coincidences is evident by the nonzero values predicted for T_{20} and T_{22} when only the $^1S_0$ and $^3S_1 - {}^3D_1$ forces are used in the calculations. The T_{20} for

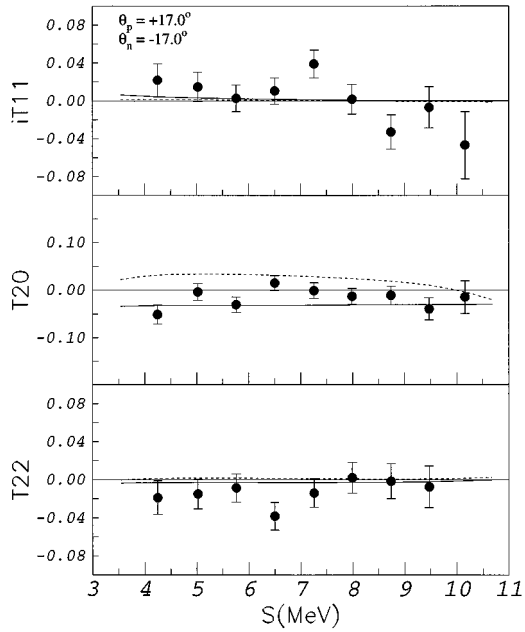

FIG. 13. Analyzing powers for pn coincidences for the $\vec{d} + d \rightarrow d + p + n$ reaction at an incident energy of 12.0 MeV. The particle angles are $\theta_p = +17.0°$ and $\theta_n = -17.0°$, and the arc length S is measured along the E_p vs E_n kinematic locus. The data are from the present measurements, and the calculations are the same as in Fig. 6.

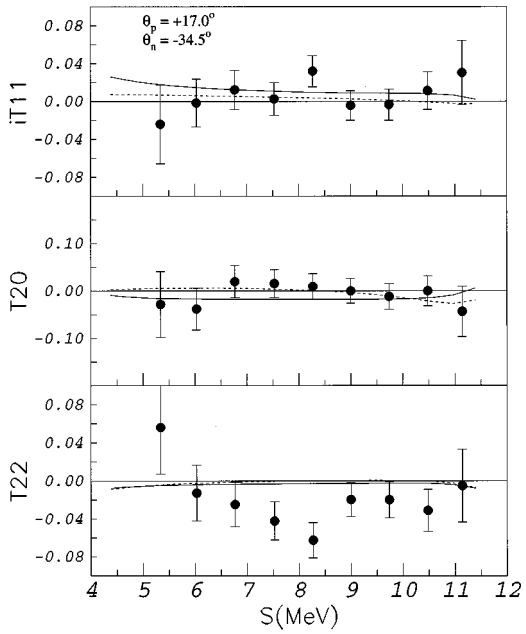

FIG. 14. The same as Fig. 13, except for particle angles $\theta_p = +17.0°$ and $\theta_n = -34.5°$.

dN coincidences also show sensitivity to the P NN forces, while the T_{22} has only a very modest dependence on the NN P forces. These results are consistent with observations in the Nd system, as is expected since our model uses a realistic description of the underlying $3N$ system. The T_{20} data for the three measured pn angle pairs are close to zero, as shown in Figs. 13–15. Zero values are intuitively expected since these np data are dominated by projectile breakup, which means that the effective incident particle is a polarized nucleon, and therefore T_{20} should be zero. Note, however, that our model predicts the T_{20} to be slightly negative. Also note that the inclusion of NN P forces has an

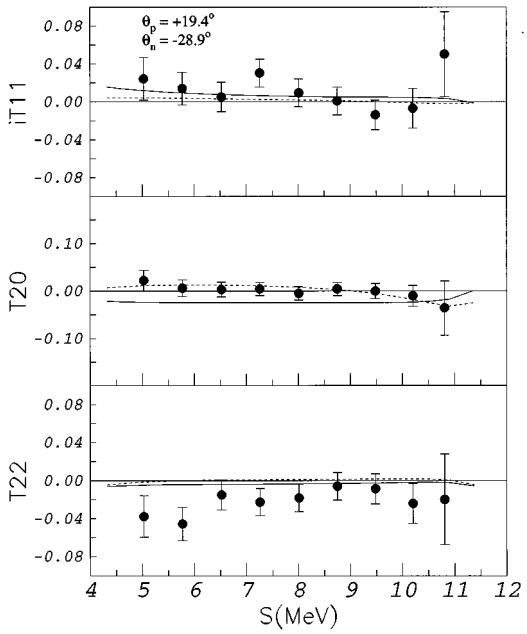

FIG. 15. The same as Fig. 13, except for particle angles $\theta_p = +19.4°$ and $\theta_n = -28.9°$.

effect. At these same angle pairs, our T_{22} data are appreciably more negative than the model predictions, which are essentially zero. The behavior of pn T_{20} and T_{22} shows the limitations of our model and indicates the importance of higher order terms.

V. CONCLUSIONS

In this paper, we report the most extensive set of measurements of vector iT_{11} and tensor T_{20} and T_{22} analyzing powers and cross sections ever made for the $d+d \rightarrow d+p+n$ reaction. Data for six dp, three dn, and three pn angle pairs for an incident deuteron energy of 12.0 MeV are compared to our IA model calculations. The main feature that distinguishes our model from older IA calculations is our theoretically exact treatment of the Nd vertices. The spin observables for this reaction are comparable in magnitude to those for nd scattering, and we have demonstrated that they can be measured to an accuracy better than ± 0.006 for a bin width of 750 keV along the S curve.

Our model gives a good description of the shape of the cross-section data at all measured angle pairs except for those kinematic conditions when one pole dominates. The iT_{11} data are quite well described with only three exceptions. The calculations differ by about five standard deviations from the data for $S<7$ MeV at the angle pair $(\theta_d = +10.0°, \theta_p = -41.2°)$, the predicted iT_{11} is systematically more positive than the data at $(\theta_d = +34.5°, \theta_p = -17.0°)$, and for the angle pair $(\theta_p = +17.0°, \theta_n = -17.0°)$, the calculations are 2.5 standard deviations from the data at $S = 7$ MeV. The calculations are in good agreement with the T_{20} data except at the angle pairs $(\theta_d = +17.0°, \theta_N = -34.5°)$ and $(\theta_d = +19.0°, \theta_n = -28.9°)$, which are the same angles where the model fails to describe the cross-section shape. Our model describes all T_{22} data quite well, except at $(\theta_p = +17.0°, \theta_n = -34.5°)$ and $(\theta_p = +19.0°, \theta_n = -28.9°)$.

Given that our model contains the essential physics of the leading terms in a full $4N$ calculation, the combined analysis of cross sections and spin observables provides insight into the interference between the QFS poles, the need to include higher order scattering terms, and the sensitivity of the observables to the underlying NN force. These data, when analyzed with full $4N$ calculations, could be important in the resolution of the Nd A_y puzzle [37], since they are also sensitive to the NN ^3P_j forces.

ACKNOWLEDGMENTS

This work was supported in part by the U.S. Department of Energy, Office of High Energy and Nuclear Physics under Grant No. DEFG05-91-ER40619, the U.S.-Croatia Joint Board Under Contract No. JF129, by the Deutsche Forschungsgemeinschaft Contract No. Me544/8-1, by the European Community Contract No. CI1*-CT-91-0894, and JNICT grant CERN/P/FAE/1047. The calculations were performed on the Cray Y-MP of the North Carolina Supercomputing Center at Research Triangle Park, North Carolina. One of us (A.C.F.) would like to thank TUNL for the hospitality during visits.

APPENDIX

At each particle angle pair, the relative cross-section and vector analyzing powers are computed at points along the kinematic locus by evaluating Eq. (13) in the main text. The inputs required to compute Eq. (13) are the half-shell nd t matrix, kinematic quantities, angular momentum coupling coefficients and the deuteron wave function. The half-shell nd t matrix elements $\langle 1\frac{1}{2}\Sigma' L';\mathbf{Q}_i|Z(\varepsilon_i)|\mathbf{Q}_i^{\pm};\Sigma L 1\frac{1}{2}\rangle$ are generated with a $3N$ code that solves the Faddeev equations using separable NN potentials. These elements are projected in the channel spin and orbital angular momentum basis, Σ and L. The $4N$ scattering amplitudes are calculated from the nd half-shell t matrix elements using the following relation:

$$\langle 1\tfrac{1}{2}\Sigma'\sigma';\mathbf{Q}_i'|Z(\varepsilon_i)|\mathbf{Q}_i^{\pm};1\tfrac{1}{2}\Sigma\sigma\rangle=\sum_{\substack{LML'M'\\JM_J}} 4\pi\ \ Y^*_{LM}(\mathbf{Q}_i^{\pm})Y_{L'M'}(\mathbf{Q}_i')\times C^{\Sigma LJ}_{\sigma MM_J}C^{\Sigma' L' J}_{\sigma' M' M_J}\langle 1\tfrac{1}{2}\Sigma' L';\mathbf{Q}_i|Z(\varepsilon_i)|\mathbf{Q}_i^{\pm};\Sigma L 1\tfrac{1}{2}\rangle. \tag{A1}$$

The unprimed and primed symbols represent quantities before and after the nd scattering vertex. The kinematic variables are defined as in the main text. The L and J are, respectively, the relative orbital angular momentum between the neutron and deuteron and the total angular momentum in the nd system. The M and M_J are their projections onto the z axis. The Σ and σ are the channel spin and its projection in the $3N$ system. The Y_{LM} and C are the spherical harmonics and Clebsch-Gordon coefficients. Four terms result from the trace of the complex amplitudes $T^\dagger T$: projectile breakup $T_1^\dagger T_1$, target breakup $T_2^\dagger T_2$, and two interference terms $T_1^\dagger T_2$ and $T_2^\dagger T_1$. Each term is evaluated using the equations that follow:

$$\begin{aligned}T_1^\dagger T_1=&\tfrac{1}{2}\sum_{\substack{\Sigma\sigma\\ \Sigma'\sigma'\\ \overline{\Sigma\sigma}}}[\langle 1\tfrac{1}{2}\Sigma'\sigma';\mathbf{Q}_1'|Z(\varepsilon_1)|\mathbf{Q}_1^{+};1\tfrac{1}{2}\Sigma\sigma\rangle\chi_d(q_1^{+})+\langle 1\tfrac{1}{2}\Sigma'\sigma';\mathbf{Q}_1'|Z(\varepsilon_1)|\mathbf{Q}_1^{-};1\tfrac{1}{2}\Sigma\sigma\rangle\chi_d(q_1^{-})]^*\\ &\times[\langle 1\tfrac{1}{2}\Sigma'\sigma';\mathbf{Q}_1'|Z(\varepsilon_1)|\mathbf{Q}_1^{+};1\tfrac{1}{2}\overline{\Sigma\sigma}\rangle\chi_d(q_1^{+})+\langle 1\tfrac{1}{2}\Sigma'\sigma';\mathbf{Q}_1'|Z(\varepsilon_1)|\mathbf{Q}_1^{-};1\tfrac{1}{2}\overline{\Sigma\sigma}\rangle\chi_d(q_1^{-})]\\ &\times 3\times\hat{k}\hat{\Sigma}\hat{1}\ (-1)^{1/2+\Sigma}C^{\Sigma k\overline{\Sigma}}_{\sigma q\sigma}\ W(\overline{\Sigma}\Sigma\ \tfrac{1}{2}\ \tfrac{1}{2};k1)W(11\tfrac{1}{2}\ \tfrac{1}{2};k\tfrac{1}{2}).\end{aligned} \tag{A2}$$

The hat over a parameter is an abbreviation for $\hat{i}=\sqrt{2i+1}$, where i represents the hatted parameter. The W is a Racah coefficient, and the χ_d is the deuteron wave function as in the main text.

$$\begin{aligned}T_2^\dagger T_2=&\tfrac{1}{2}\sum_{\substack{\Sigma\sigma\\ \Sigma'\sigma'\\ \overline{\Sigma\sigma}}}[\langle 1\tfrac{1}{2}\Sigma'\sigma';\mathbf{Q}_2'|Z(\varepsilon_2)|\mathbf{Q}_2^{+};1\tfrac{1}{2}\Sigma\sigma\rangle\chi_d(q_2^{+})+\langle 1\tfrac{1}{2}\Sigma'\sigma';\mathbf{Q}_2'|Z(\varepsilon_2)|\mathbf{Q}_2^{-};1\tfrac{1}{2}\Sigma\sigma\rangle\chi_d(q_2^{-})]^*\\ &\times[\langle 1\tfrac{1}{2}\Sigma'\sigma';\mathbf{Q}_2'|Z(\varepsilon_2)|\mathbf{Q}_2^{+};1\tfrac{1}{2}\overline{\Sigma\sigma}\rangle\chi_d(q_2^{+})+\langle 1\tfrac{1}{2}\Sigma'\sigma';\mathbf{Q}_2'|Z(\varepsilon_2)|\mathbf{Q}_2^{-};1\tfrac{1}{2}\overline{\Sigma\sigma}\rangle\chi_d(q_2^{-})]\\ &\times\tfrac{3}{2}\hat{1}\hat{k}\hat{\Sigma}W(\Sigma 1\overline{\Sigma 1};\tfrac{1}{2}k)\ C^{\Sigma k\overline{\Sigma}}_{\sigma q\sigma}(-1)^{k+\overline{\Sigma}+1/2},\end{aligned} \tag{A3}$$

$$\begin{aligned}T_1^\dagger T_2=&\tfrac{1}{2}\sum_{\substack{\Sigma\sigma\\ \Sigma'\sigma'\\ \overline{\Sigma\sigma}\\ \overline{\Sigma'\sigma'}}}[\langle 1\tfrac{1}{2}\Sigma'\sigma';\mathbf{Q}_1'|Z(\varepsilon_1)|\mathbf{Q}_1^{+};1\tfrac{1}{2}\Sigma\sigma\rangle\chi_d(q_1^{+})+\langle 1\tfrac{1}{2}\Sigma'\sigma';\mathbf{Q}_1'|Z(\varepsilon_1)|\mathbf{Q}_1^{-};1\tfrac{1}{2}\Sigma\sigma\rangle\chi_d(q_1^{-})]^*\\ &\times[\langle 1\tfrac{1}{2}\overline{\Sigma'}\overline{\sigma'};\mathbf{Q}_2'|Z(\varepsilon_2)|\mathbf{Q}_2^{+};1\tfrac{1}{2}\overline{\Sigma\sigma}\rangle\chi_d(q_2^{+})+\langle 1\tfrac{1}{2}\overline{\Sigma'}\overline{\sigma'};\mathbf{Q}_2'|Z(\varepsilon_2)|\mathbf{Q}_2^{-};1\tfrac{1}{2}\overline{\Sigma\sigma}\rangle\chi_d(q_2^{-})]\\ &\times 3\hat{1}\hat{k}\hat{\Sigma}\hat{\Sigma}'\sum_{\substack{ABCD\\ abcd}}\hat{A}^2\hat{B}^2\hat{C}^2\hat{D}(-1)^{1-\Sigma-\Sigma'-\overline{\Sigma}-1/2-D}\times C^{\Sigma' A\overline{\Sigma'}}_{\sigma' a\sigma'}\ C^{\Sigma D\overline{\Sigma}}_{\sigma d\sigma}\ C^{AkD}_{aqd}\ \ W\langle\tfrac{1}{2}\overline{\Sigma'}\ \tfrac{1}{2}\Sigma';1A)\\ &\times W(\tfrac{1}{2}\Sigma\ \tfrac{1}{2}\ \tfrac{1}{2};1B)\begin{Bmatrix}\frac{1}{2} & C & \overline{\Sigma}\\ 1 & k & 1\\ \frac{1}{2} & B & \frac{1}{2}\end{Bmatrix}\begin{Bmatrix}\overline{\Sigma} & D & \Sigma\\ \frac{1}{2} & A & \frac{1}{2}\\ C & k & B\end{Bmatrix}.\end{aligned} \tag{A4}$$

The array within the large bracket denotes a ''9j'' symbol. In all equations the variables A, B, C, and D are constrained by the usual triangular relations of angular momentum algebra.

$$T_2^\dagger T_1 = \tfrac{1}{2} \sum_{\substack{\Sigma\sigma \\ \Sigma'\sigma' \\ \overline{\Sigma}\sigma \\ \overline{\Sigma'}\overline{\sigma'}}} 3\hat{k}\hat{\Sigma}'\hat{\Sigma}\hat{1} \sum_{\substack{Aa \\ Bb}} \hat{A}^2\hat{B}\ C^{\Sigma' A\overline{\Sigma'}}_{\sigma' a\sigma'}\ C^{AB\overline{\Sigma}}_{ab\sigma}\ C^{\Sigma kB}_{\sigma qb}(-1)^{B-\Sigma-\overline{\Sigma}-\Sigma'}\ W(\tfrac{1}{2}\overline{\Sigma'}\,\tfrac{1}{2}\Sigma';1A)$$

$$\times W(B\,\tfrac{1}{2}k1;1\Sigma) \begin{Bmatrix} \frac{1}{2} & B & 1 \\ 1 & \overline{\Sigma} & \frac{1}{2} \\ \frac{1}{2} & A & \frac{1}{2} \end{Bmatrix} \times [\langle 1\tfrac{1}{2}\Sigma'\sigma';\mathbf{Q}_2';|Z(\varepsilon_2)|\mathbf{Q}_2^+;1\tfrac{1}{2}\Sigma\sigma\rangle\chi_d(q_2^+)$$

$$+\langle 1\tfrac{1}{2}\Sigma'\sigma';\mathbf{Q}_2'|Z(\varepsilon_2)|\mathbf{Q}_2^-;1\tfrac{1}{2}\Sigma\sigma\rangle\chi_d(q_2^-)]^*[\langle 1\tfrac{1}{2}\overline{\Sigma'}\,\overline{\sigma'};\mathbf{Q}_1'|Z(\varepsilon_1)|\mathbf{Q}_1^+;1\tfrac{1}{2}\overline{\Sigma\sigma}\rangle\chi_d(q_1^+)$$

$$+\langle 1\tfrac{1}{2}\overline{\Sigma'}\,\overline{\sigma'};\mathbf{Q}_1'|Z(\varepsilon_1)|\mathbf{Q}_1^-;1\tfrac{1}{2}\overline{\Sigma\sigma}\rangle\chi_d(q_1^-)]. \tag{A5}$$

[1] O. A. Yakubovsky, Sov. J. Nucl. Phys. **5**, 937 (1967).

[2] E. O. Alt, P. Grassberger, and W. Sandhas, Phys. Rev. C **1**, 85 (1970).

[3] A. C. Fonseca, Phys. Rev. Lett. **63**, 2036 (1989).

[4] T. E. Mdlalose, H. Fiedeldey, and W. Sandhas, Nucl. Phys. **A457**, 273 (1986).

[5] W. Glöckle, H. Kamada, H. Witała, D. Hüber, and J. Golak, in *Few-Body Problems in Physics*, Williamsburg, VA, 1994, edited by F. Gross, AIP Conf. Proc. No. 334 (AIP, New York, 1995), p. 45; H. Kamada and W. Glöckle, Nucl. Phys. **A548**, 205 (1992); H. Kamada and W. Glöckle, Phys. Rev. Lett. **71**, 971 (1993); W. Glöckle and H. Kamada, Nucl. Phys. **A560**, 541 (1993).

[6] H. M. Hofmann, Nucl. Phys. **A416**, 363 (1984); H. Kanada, T. Kaneko, and Y. C. Tang, Phys. Rev. C **43**, 371 (1991).

[7] G. M. Hale, R. E. Brown, and N. Jarmie, Phys. Rev. Lett. **59**, 763 (1987).

[8] J. Carlson, Phys. Rev. C **38**, 1879 (1988); Nucl. Phys. **A508**, 141c (1990).

[9] A. Kievsky, M. Viviani and S. Rosati, Nucl. Phys. **A551**, 241 (1993); **A577**, 511 (1994); Phys. Rev. C **52**, R15 (1995); M. Viviani, A. Kievsky, and S. Rosati, in *Few-Body Problems in Physics* [5], p. 844.

[10] I. Šlaus, R. Machleidt, W. Tornow, W. Glöckle, and H. Witała, Comments Nucl. Part. Phys. **20**, 85 (1991).

[11] G. H. Bertold, A. Stadtler, and H. Zankel, Phys. Rev. C **41**, 1365 (1990); H. -P. Kotz, Ch. Brandstatter, W. Plessas, and G. Berthold, in *Few-Body Problems in Physics* [5], p. 482; A. C. Fonseca, Few-Body Syst. Suppl. **7**, 177 (1994).

[12] E. O. Alt and M. Rauch, Phys. Rev. C **49**, R2285 (1994).

[13] B. J. Wielinga, A. D. IJpenberg, K. Mulder, R. van Dantzig, and I. Šlaus, Phys. Rev. Lett. **27**, 1229 (1971).

[14] E. Andrade, V. Valkovic, D. Rendic, and G. C. Phillips, Nucl. Phys. **A183**, 145 (1972); V. Valkovic, I. M. Duck, and G. C. Phillips, *ibid.* **A183**, 126 (1972); V. Valkovic, N. Gabitzsch, D. Rendic, I. M. Duck, and G. C. Phillips, *ibid.* **A182**, 225 (1972).

[15] D. I. Bonbright, R. G. Allas, R. O. Bondelid, E. L. Petersen, A. G. Pieper, R. B. Theus, and I. Šlaus, Phys. Rev. C **8**, 114 (1973).

[16] V. Valkovic, I. M. Duck, and G. C. Phillips, Phys. Lett. **42B**, 191 (1972).

[17] P. F. Donovan, Rev. Mod. Phys. **37**, 501 (1965).

[18] T. Tanabe, J. Phys. Soc. Jpn. **25**, 21 (1968).

[19] H. Brückmann, W. Gehrke, W. Kluge, H. Matthay, L. Schanzler, and K. Wick, Z. Phys. **217**, 350 (1968).

[20] J. P. Burq, J. C. Cabrillat, M. Chemarin, B. Ille, and G. Nicolai, Nucl. Phys. **A179**, 385 (1972).

[21] A.D. Ijpenberg, R. van Dantzig, B.J. Wielinga, and I. Slaus, *Few Particle Problems*, edited by I. Šlaus *et al.* (North Holland, Amsterdam, 1972), p. 651.

[22] A. Djaloeis, J. Bojowald, C. Alderliesten, C. Mayer-Boricke, G. Paic, and Z. Bajzer, Nucl. Phys. **A273**, 29 (1976).

[23] W. Kluge, H. Matthay, R. Schlufter, H. Schneider, and K. Wick, Nucl. Phys. **A302**, 93 (1978).

[24] K. Fukunaga, T. Ohsawa, S. Kakigi, A. Okihana, S. Tanaka, T. Sekioka, and H. Nakamura-Yokota, Nucl. Phys. **A390**, 19 (1982).

[25] C. R. Howell *et al.*, Phys. Rev. Lett. **61**, 1565 (1988).

[26] K. Fukunaga, S. Kakigi, T. Ohsawa, A. Okihana, T. Sekioka, H. Nakamura-Yokota, T. Murayama, and T. Hayashi, Few-Body Syst. **7**, 119 (1989).

[27] C. R. Howell *et al.*, Phys. Rev. C **48**, 2855 (1993).

[28] P. D. Felsher, Ph.D. thesis, Duke University, 1991.

[29] T. Clegg, G. Bissinger, and T. Trainor, Nucl. Instrum. Methods **120**, 445 (1974).

[30] G. G. Ohlsen and P. W. Keaton, Jr., Nucl. Instrum. Methods **109**, 41 (1973).

[31] W. Haeberli, in *Nuclear Spectroscopy and Reactions*, edited by J. Cerny (Academic, New York, 1974), Pt. A, p. 151.

[32] G. G. Ohlsen, Technical Report No. LA-4451, Los Alamos Scientific Laboratory of the University of California, 1970.

[33] G. G. Ohlsen, R. E. Brown, F. D. Correll, and R. A. Hardekopf, Nucl. Instrum. Methods **179**, 283 (1981).

[34] J. A. McIntyre, P. H. Beatty, J. D. Bronson, R. J. Hastings, J. G. Rogers, and M. S. Shaw, Phys. Rev. C **5**, 1796 (1972).

[35] A. C. Phillips, Nucl. Phys. **A107**, 209 (1968).

[36] F. D. Correll, G. G. Ohlsen, R. E. Brown, R. A. Hardekopf, M. Jarmie, and P. Doleschall, Phys. Rev. C **23**, 960 (1981).

[37] C. R. Howell *et al.*, Few-Body Syst. **2**, 19 (1987).